

Effective Conductivity of Cu-Fe and Sn-Al Miscibility Gap Alloys

Authors

*Anthony J. Rawson, University of Newcastle

Prof. Erich Kisi

Dr. Heber Sugo

Dr. Thomas Fiedler

*Corresponding Author

Keywords

Miscibility Gap Alloy

Effective Thermal Conductivity

Thermal Storage

Lattice Monte Carlo

Microstructural Efficiency

Abstract

The effective thermal conductivity of Cu-Fe and Sn-Al miscibility gap alloys over a range of temperatures and volume fractions was determined using the Lattice Monte Carlo Method. The Cu-Fe system was found to have an effective conductivity predictable by the Maxwell-Eucken Model. The Sn-Al system was not consistent with any empirical model analysed. The microstructures of physical samples were approximated using a random growth algorithm calibrated to electron or optical microscope images. Charts of effective conductivity against temperature for a number of volume fractions are presented for the two alloys. It was determined that the Cu-Fe alloy would benefit from an interstice type microstructure and the Sn-Al would be more efficient with a hard spheres type microstructure. More general conclusions are drawn about the efficiency of the two observed microstructures.

1 Introduction

Processes that utilise intermittent heat resources stand to benefit considerably from a high energy density heat storage device. These processes may use the heat directly or through a power cycle transform the heat into electrical energy. For example power generation through concentrated solar thermal (CST) generation may overcome intermittency of the radiation source given an adequate heat storage device.

Heat storage devices relying on a sensible method, by definition, deliver energy at a range of temperatures. Additionally the energy density is limited by the volumetric heat capacity of the material. Heat storage devices that incorporate a solid to liquid phase change benefit from the latent heat required (or available) in melting (or freezing) a material. A great number of materials incorporating a phase change have been identified and categorised on transition temperature [1-3]. Knowledge of how the materials behave thermally is paramount to their successful adoption.

Most purely latent heat storage materials suffer from a number of limitations typically involving their low thermal conductivity, thermal stability and reactivity. As a consequence of these limitations a new range of thermal storage materials have been developed that take advantage of the favourable thermal properties of metals.

Miscibility gap alloys (MGAs) are capable of storing thermal energy with high energy density and high thermal conductivity [4]. The alloys consist of a distributed metallic phase surrounded by another phase with a higher melting temperature. The two (or more) metals must be strongly immiscible to prevent the formation of solid solutions or intermetallics. The distributed phase may then freeze or melt, releasing or storing a large amount of thermal energy at a temperature without degradation of the system.

The microstructure of these MGAs consists of a dispersed fusible phase in a highly conductive solid matrix [4]. Efficient design of thermal storage devices employing MGAs necessitates knowledge of their effective thermal

conductivity, specific heat capacity and density. The storage capacity and charge/discharge rates for the material may be determined and thus a device rated to an application. The wide range of volume fractions, morphologies and constituent thermal conductivities encountered in the different MGAs warrant an advanced approach to estimating the effective thermal properties aforementioned.

The two MGAs of interest in this paper are the Copper-Iron and Tin-Aluminium systems (Fusible Phase-Matrix Phase). Though the thermal properties of the constituents are well understood and documented [5, 6], the properties of the *alloy* at differing composition are more uncertain. This research addresses existing methods of numerically evaluating the properties of the alloys and proposes the use of the Lattice Monte Carlo (LMC) method as a viable means of predicting the Effective thermal conductivity for the thermal storage systems.

1.1 Effective Thermal Properties of Composites

The thermal properties of concern for heat transfer modelling of a solid are isobaric specific heat capacity, density and thermal conductivity. Each of these properties should be considered temperature dependent. On phase change the thermal properties are often found to change significantly. It may be readily shown that effective specific heat capacity for a composite is the mass fraction weighted average of the component heat capacities. The effective density of a composite is the volume fraction weighted average of the component densities.

In contrast to these scalar properties, thermal conductivity is influenced by more than the constituent properties and relative amounts of the components in a composite. Shape, distribution and orientation of the phases all contribute to the effective conductivity of the material [7]. A great quantity of literature exists on determining the thermal conductivity of composites from both theoretical and experimental bases [8].

The alloys considered in this paper have been found experimentally to have differing microstructures [4]. The Cu-Fe systems display a dispersion of near spherical inclusions of copper that may touch and intersect. The Sn-Al alloys have a microstructure where the fusible Tin looks to have flowed and filled the interstices between larger spherical Aluminium particles. These characteristics are shown in (Figure 1):

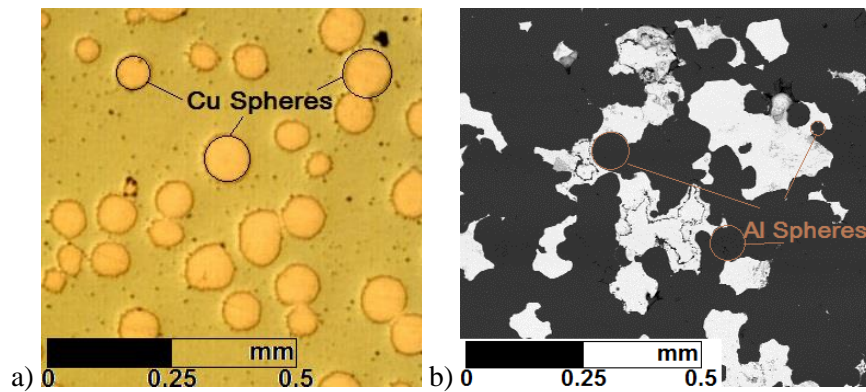


Figure 1 Morphology of Cu-Fe (a) and Sn-Al (b) microstructures. (a) is an optical microscope image whilst (b) is an SEM image. The Cu-Fe alloy appears to resemble a random distribution of spheres. The Sn-Al alloy appears to resemble an interstice filling type structure.

Regardless of the morphology, the effective conductivity is known to always fall within the Wiener bounds [9] given by the volume fraction weighted series and harmonic averages. Here k refers to conductivity, φ to volume fraction and the subscripts A and B refer to the fusible and matrix phases respectively.

$$\bar{k}_{ser} = \varphi_A k_A + \varphi_B k_B \quad (1)$$

$$\bar{k}_{har} = \left(\frac{\varphi_A}{k_A} + \frac{\varphi_B}{k_B} \right)^{-1} \quad (2)$$

The Maxwell-Eucken (ME1) model has been used to estimate the effective conductivity of a small dispersion of spheres in a matrix [10, 11]. The model assumes the temperature fields about each particle do not interact [7]. A relatively sparse distribution of spheres, like the apparent morphology of the Cu-Fe alloy, is likely to be predicted by this model.

$$\bar{k}_{ME1} = \frac{k_A \varphi_A + k_B \varphi_B [3k_A / (2k_A + k_B)]}{\varphi_A + \varphi_B [3k_A / (2k_A + k_B)]} \quad (3)$$

The Maxwell-Eucken model has been modified (ME2) to also estimate the other extreme of a large volume fraction of particles by interchange of the A and B phases in equation 3 [12].

$$\bar{k}_{ME2} = \frac{k_B \varphi_B + k_A \varphi_A [3k_B / (2k_B + k_A)]}{\varphi_B + \varphi_A [3k_B / (2k_B + k_A)]} \quad (4)$$

Another model commonly utilised assumes a macroscopically isotropic distribution of components and has an implicit solution. The effective mean field theory was first proposed by Bruggeman in 1935 [13]. The effective conductivity is found on an implicit solution of the following.

$$(1 - \varphi_B) \frac{k_A - \bar{k}_{EMT}}{k_A + 2\bar{k}_{EMT}} + \varphi_B \frac{k_B - \bar{k}_{EMT}}{k_B + 2\bar{k}_{EMT}} = 0 \quad (5)$$

A more recent model discussed by del Rio et. al. in 1998 [14] estimates effective conductivity through approximately satisfying the reciprocity conditions (developed by Keller in 1964 [15] for 2d systems of parallel cylinders) of statistically equivalent binary components. Here the ratio of conductivities was given as $r = k_B/k_A$. The following model is referred to as the reciprocity model in this paper.

$$\bar{k}_{rec} = k_A \frac{1 + \varphi_A (r^{0.5} - 1)}{1 + \varphi_A (r^{-0.5} - 1)} \quad (6)$$

Though grounded in either geometric or statistical theory all of these five models are independent of the shape, distribution and orientation of inclusions. Thus they are limited to a particular subset of microstructures. Many additional models exist that take into account these factors but as each cater for only a specific range of shapes and materials they have little generality [8]. In addition to calculating the effective thermal conductivity of the Cu-Fe and Sn-Al alloys we also seek to identify which, if any, of the models described suit each microstructure type.

To better observe how altering a microstructure might optimise thermal conductivity a property was developed called microstructural efficiency. This was defined as the ratio of the effective conductivity to the series average. This is described mathematically below.

$$\eta_{micro} = \frac{k_{eff}}{\bar{k}_{ser}} = \frac{k_{eff}}{\varphi_A k_A + \varphi_B k_B} \quad (7)$$

1.2 Numerical Estimation of Effective Thermal Conductivity

Lattice Monte-Carlo (LMC) analysis is a multi-scale modelling method for complex diffusion problems [16]. Complex geometries with varying conductivity are decomposed to a grid which virtual entities of energy or mass may explore. In a heat transfer problem the entities are considered to represent energy and they diffuse, free of potential, in a random walk. After a known period of time, the displacements of a very large number of particles are recorded. The isotropic and tensor components of conductivity are proportional to the ensemble averaged displacement $\langle R^2 \rangle$ and the length of time t over which they were permitted to wander as described in equation 8. The LMC method has been used successfully in heat transfer problems for multiphase composites [17-19]

$$k \propto \frac{\langle R^2 \rangle}{t} \quad (8)$$

If the dominant heat transfer mechanism can be assumed to be conduction, the LMC method is ideal for estimating the effective thermal conductivity of regular and irregular composite microstructures like those of an MGA. The LMC method was preferred over finite element methods due to its accuracy, inherent tensorial output and computational efficiency for steady state simulations. If a transient analysis was required a finite element simulation would generally be more computationally efficient. Obtaining these relationships is of interest in modelling MGAs at the macroscopic scale using effective properties.

The LMC procedure described above requires a lattice on which to run. This lattice prescribes the location, relative size and shape of inclusions and also indicates the conductivity of each phase. The virtual energy particles are allowed to diffuse over the lattice with a probability described by the current and target node conductivities. The LMC steady state procedure simulates the effective conductivity of an infinite number of repeating cells. These cells are chosen to be sufficiently large with respect to the inclusion dimensions so that any artificial structuring from the periodic

boundaries has a negligible influence on effective conductivity. Provided the lattice node density is great enough to adequately resolve the shape of the randomly placed inclusions, the simulated effective conductivity will be independent of inclusion size. That is, the effective conductivity for an infinite random microstructure is dependent on inclusion shape, orientation and packing; not on physical inclusion size.

The complete microstructure of a physical specimen is difficult to transform into a digital format suitable for LMC simulations. Techniques utilising X-Ray tomography to non-destructively import the 3 dimensional spatial data exactly have been used in a wide variety of fields [20, 21]. Where this technique is not available the microstructure may be ‘grown’ with information taken from 2 dimensional slices of the real microstructure. The algorithm which builds the microstructure may be called a Random Microstructure Generation (RMG) Algorithm.

The quality of the generated microstructure may be inferred through comparison of a number of correlation functions including the radial distribution and the two point probability functions as outlined in Torquato’s text [7]. The radial distribution function generates a curve indicating the fraction of the inclusion phase in sequential shells from the centre of each inclusion. The two point probability function generates a curve of the likelihood that a line of length R will have both its vertices within the same phase. These functions are performed on 2d images from optical or electron microscopy or on slices from generated microstructures. Analysing the variance between two curves for the data range gives a quantitative means of characterising spatial arrangements of constituents.

The use of an LMC method on a RMG algorithm domain results in uncertainty in the simulated property. The uncertainty may be further classified as systematic or statistical. Systematic errors stem from periodic boundary interactions (size of repeating cell) and lattice sizing (decomposition of curvature). Statistical errors are inherent in the LMC method and can be minimised by increasing the number of particles and number of time steps in the analysis. External to the LMC method considerable uncertainties will likely exist in the constituent conductivities.

An LMC simulation utilises a base cell with periodic boundaries. This base cell must be large enough, relative to the inclusion geometry, to avoid returning a perturbed conductivity for the ideally random microstructure. Above a certain critical cell size the standard deviation of simulated conductivity reaches a constant value. The critical cell size describes the smallest domain on which the LMC simulation can run whilst still eliminating the systematic error introduced by periodic boundaries.

As with Finite Element techniques the LMC mesh must be fine enough to properly capture the geometric detail of the system. Regions of curvature, common in the microstructures of this research, require a high node density (when the grid is cubic) to be successfully captured in the mesh. Again, as the parameter of interest is thermal conductivity, the mesh should be fine enough such that an acceptably small variation in the LMC conductivity output is obtained.

Statistical uncertainty in the LMC process arises from the finite number of particles and time involved in the simulation. The particles must be allowed to diffuse for a long enough time whereby an adequate portion of the medium is explored. Similarly, a large number of particles must be simulated such that a great number of different possible diffusion paths are represented in the simulation.

1.3 Dominant Heat Transfer Mechanism

Random heterogeneous systems are considered isolated from the environment for analysis of effective thermal conductivity. The heat transfer mechanisms within the medium available are conduction, natural convection and radiation off the inclusion walls. All metals in both solid and molten states are completely opaque, hence radiation can be neglected. Given the small size of inclusions, small temperature gradients across inclusions and the low thermal expansivity of the molten metals, the contribution to effective thermal conductivity from natural convection would be expected to be low.

The dimensionless Rayleigh number is often used to describe the relative magnitude of buoyant and viscous forces in a fluid [22]. It is dependent on both fluid and geometry properties as the product of Prandtl and Grashof numbers.

$$Pr = \frac{\nu}{\alpha} \quad (9)$$

$$Gr = \frac{g\beta(T_s - T_\infty)L^3}{\nu^2} \quad (10)$$

$$Ra = Pr \times Gr = \frac{g\beta(T_s - T_\infty)L^3}{\nu\alpha} \quad (11)$$

Here ν is the kinematic viscosity, α the thermal diffusivity, g gravitational acceleration, β volume expansivity, T_s surface temperature, T_∞ bulk fluid temperature and L is a characteristic length (radius in this case). The Prandtl, Grashof and Rayleigh numbers are denoted by Pr , Gr and Ra respectively.

It has been shown that when the Rayleigh number is less than 100, the heat transfer in a sphere of fluid would be dominated by conduction and result in a negligible velocity field [23]. Within a cube the limit has been shown to be nearer to $Ra=3000$ [24]. For the molten metals considered in this study the inclusions would have to approach a seven millimetre diameter to exceed the critical Rayleigh number of 100 with a temperature difference of 10 °C.

A non-negligible velocity field may occur where inclusions manage to touch (percolate) and create long chains of molten metal. This is more likely at high volume fractions ($\phi_A > 0.6$) and with interstice type morphology. It is still expected that given the very small temperature gradients available during charging or discharging the transport via natural convection would be quite low. The impact of natural convection on effective thermal conductivity does not form part of this work.

2 Results and Discussion

2.1 Periodicity and Mesh Density Independence

A Matlab® program was written to generate representative microstructures for the LMC program. The random microstructure generation program for the microstructures discussed in this paper utilised spheres with a specified base radius (R) and deviation (δR). The base radius was fixed as a proportion of the base cell size at the critical periodicity fraction (as demonstrated in Figure 2 and Figure 3). The spheres allowable radial intersection was specified with an intersection parameter (I_n) and the likelihood for sphere growth via percolation (touching or intersecting another sphere) was specified with a percentage (Pe).

The parameters required as arguments for the random microstructure generation RMG were estimated by analysis of the real world microstructural images. Mean radius was provided such that periodicity and mesh independence were satisfied. The three remaining parameters controlling deviation, intersection and likelihood to percolate were set to zero or very low values for hard sphere type microstructures and were tuned for interstice type microstructures.

Given the LMC procedure utilised periodic boundaries over a base cell, the base cell had to be of sufficient size to avoid representing a periodic microstructure. A previous study looked at a random distribution of inclusions with voxel (single element) volume and established that a three dimensional structure with size 100^3 nodes was adequate to avoid periodic perturbations [17]. Given that the inclusions assessed in this work are spherical or spherical interstices made up of many nodes (many voxels volume) the study was repeated with the goal of determining a critical ratio between cell dimension and inclusion base dimension.

A volume fraction of 20% was found to create the largest systematic errors from cell size in the work of Fiedler et. al. [17]. This volume fraction was considered for the hard sphere analysis of this paper. Ten microstructures were grown for each cell size with the same generation parameters. The effective conductivity was obtained for each microstructure and the standard deviation calculated between those of the same cell size as shown in Figure 2. The critical cell size to inclusion radius was found to be around 16 for hard spheres. Beyond this ratio the standard deviation of conductivity measurements was almost constant at about one half the statistical uncertainty of the LMC process.

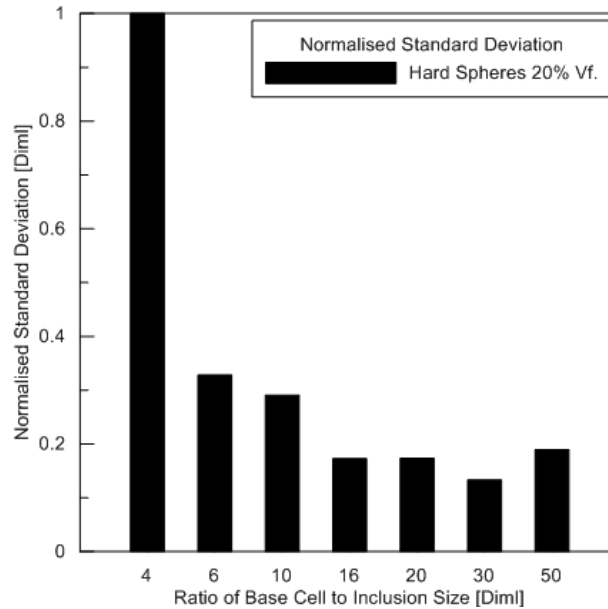


Figure 2 The Normalised Standard Deviation of effective conductivity for hard spheres (20% Vf.).

A ratio of 16 times the base radius of matrix material was found to minimise the standard deviation to near constant for the alternate morphology of interstices. The analysis was repeated for a microstructure with a range of volume fractions. The results of this are shown in Figure 3.

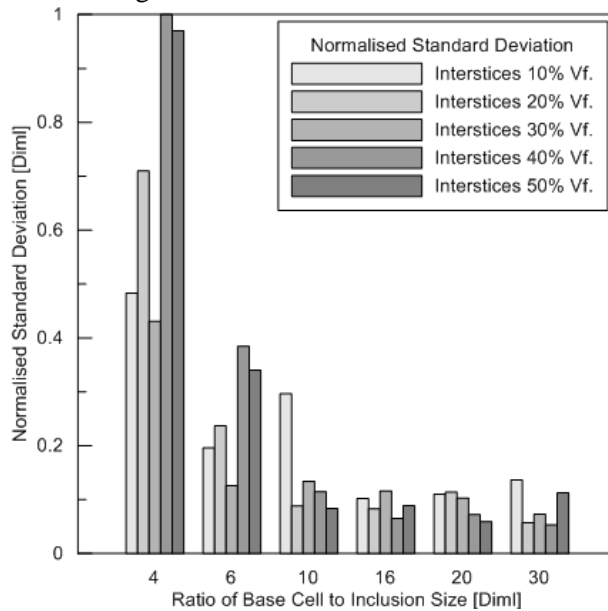


Figure 3 The Normalised Standard Deviation of effective conductivity for interstices over a range of volume fractions.

The second source of systematic error, mesh density, was also analysed by first randomly generating a typical 3 dimensional microstructure for both hard spheres and interstices. This microstructure was saved as centre and radius data only before it was decomposed upon grids with varying nodal density as shown in Figure 4. The conductivity was obtained using the LMC method for each mesh density, the density at which the conductivity became constant was determined to be the critical mesh density. This is presented as the number of nodes across the base radius.

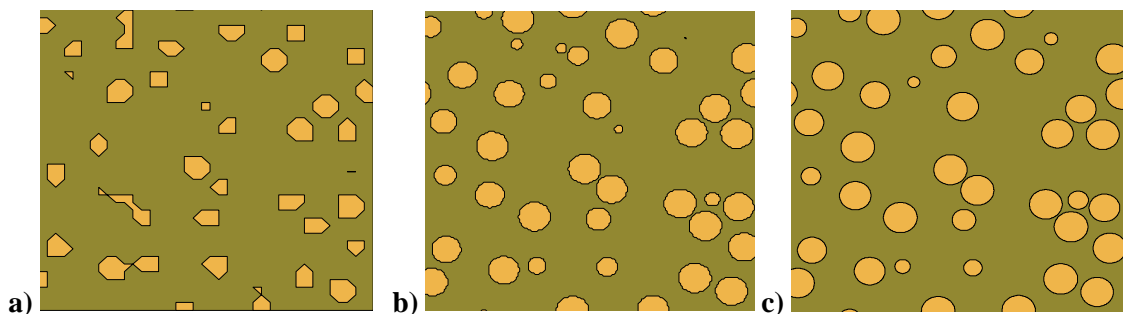


Figure 4 Increasing mesh density on a slice midway through the simulation domain for 20% inclusion volume fraction of hard spheres. a) 2 nodes across base radius, b) 10 nodes across base radius, c) 50 nodes across base radius.

It was found that for hard spheres a minimum number of 10 nodes across the inclusion base radius were necessary to eliminate the mesh error. Too few nodes could not capture the detail of the inclusion curvature. The results of the analysis are presented in Figure 5.

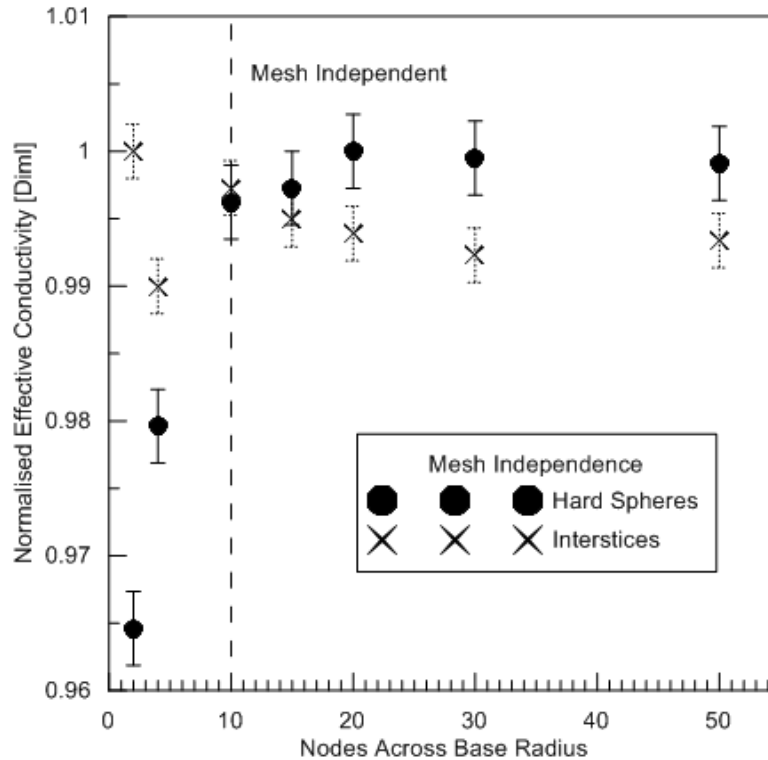


Figure 5 Normalised Effective Conductivity for 20% Volume Fraction of Hard Spheres and 35% Volume Fraction of Interstices. Those to the right of the dashed vertical line are considered mesh independent.

For inclusion type microstructures the mesh utilised could also be quite coarse without a large change in the effective conductivity. The influence of increasing mesh density on the appearance of the generated microstructure is shown in Figure 6. Ten nodes across the inclusion base radius was the lowest resolution at which the conductivity fell within the statistical uncertainty for any increase in node number as indicated in Figure 5.

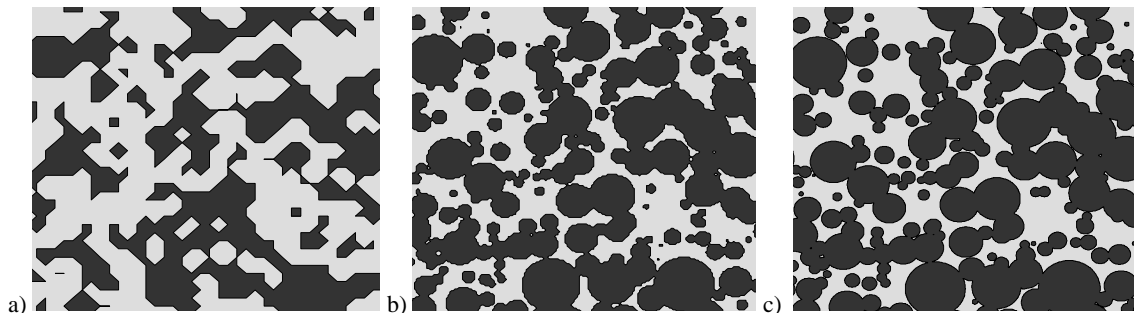


Figure 6 Increasing mesh density on a slice midway through the simulation domain for 35% inclusion volume fraction of interstices. a) 2 nodes across base radius, b) 10 nodes across base radius, c) 50 nodes across base radius.

2.2 Real and Generated Microstructures

The samples were prepared by mixing and pressing a mixture of metal powders into a specially designed canister. The Sn-Al samples were fired at 500 °C for 1 hour and the Cu-Fe samples at 1000 °C for 2 hours under an inert atmosphere. Physical samples were sectioned then wet ground and polished to a 6 µm diamond finish for metallurgical optical images and 1 µm for Back Scattered Electron (BSE) images. Optical images were then taken using an Olympus BX60M Microscope. BSE images were collected on a Philips XL-30 SEM. These images were fed into an image processing routine written in Matlab® which converted the images to a binary map upon which two point correlation functions could be performed. These functions were then used to characterise the physical specimens and compare them quantitatively to their generated equivalents.

The Copper-Iron microstructure had copper particles quite regular in size and shape. The samples were sintered below the melting temperature of copper and hence this discrete phase did not have the mobility of a liquid whilst the matrix sintered. The generated microstructures were found to have very similar radial distribution and two point probability to the real microstructures. The correlation functions variance between real and RMG was comparable in most cases

to the variance observed between real images. Typical microstructures of both real and generated microstructures are shown along with their generation properties and correlation function variances in Table 1.

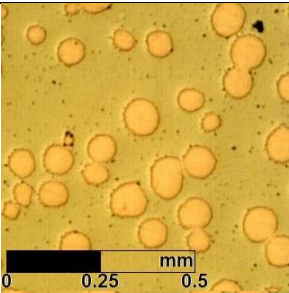
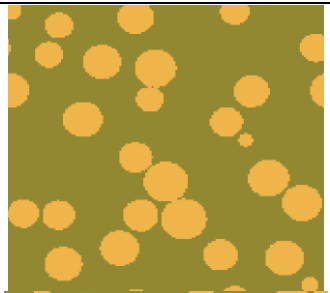
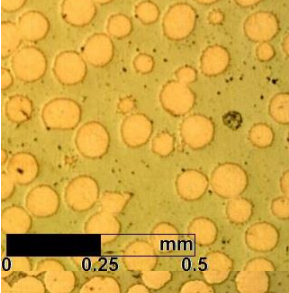
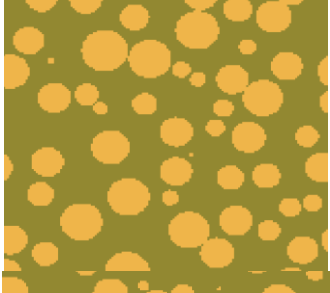
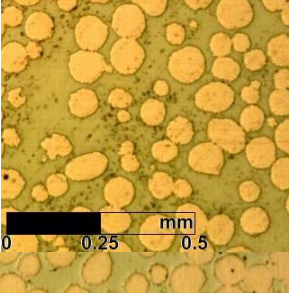
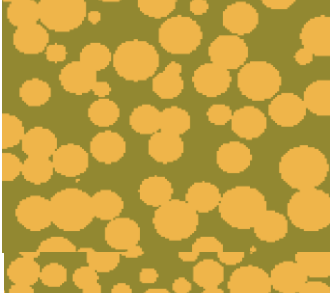
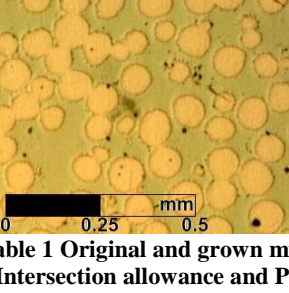
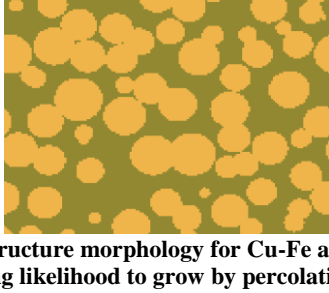
Original Microstructure	Generated Microstructure	Properties	Correlation Function Mean Variance Between Real Images	Correlation Function Mean Variance Between Real and Grown Images
		Alloy Properties: Cu-Fe 20% Vf. Generation Properties: $\delta R = 20\%$ $I_n = 0\%$ $Pe = 50\%$	Radial Distribution: 2.58×10^{-4} Two Point: 3.27×10^{-4}	Radial Distribution: 6.37×10^{-4} Two Point: 7.34×10^{-4}
		Alloy Properties: Cu-Fe 40% Vf. Generation Properties: $\delta R = 20\%$ $I_n = 0\%$ $Pe = 50\%$	Radial Distribution: 7.44×10^{-4} Two Point: 7×10^{-4}	Radial Distribution: 7.77×10^{-4} Two Point: 5.83×10^{-4}
		Alloy Properties: Cu-Fe 50% Vf. Generation Properties: $\delta R = 20\%$ $I_n = 15\%$ $Pe = 25\%$	Radial Distribution: 8.85×10^{-4} Two Point: 8.56×10^{-4}	Radial Distribution: 4.18×10^{-5} Two Point: 1.39×10^{-5}
		Alloy Properties: Cu-Fe 60% Vf. Generation Properties: $\delta R = 20\%$ $I_n = 15\%$ $Pe = 25\%$	Radial Distribution: 8.20×10^{-4} Two Point: 1.1×10^{-3}	Radial Distribution: 2.93×10^{-5} Two Point: 4.73×10^{-5}

Table 1 Original and grown microstructure morphology for Cu-Fe alloys with the generation parameters δR being Radial Deviation, I_n Intersection allowance and Pe being likelihood to grow by percolation. The mean variance between the generated and the real image correlation functions is given along with the mean variance observed between real images.

The quality of the Cu-Fe generated microstructures was found to be quite high as indicated in Table 1. Graphical representations of slices of the grown 3d structure were visually similar to the real optical micrographs. The radial distribution and two point correlation functions were also very similar between real and generated images. The similarity is reflected in the comparable average variances between these function. This suggests that the shape of the inclusions and their distribution were realistic in the grown microstructures.

The microstructure observed for the Sn-Al alloy, which was sintered above the melting temperature of tin, was rather different to the Cu-Fe alloy. The Tin phase had flowed to fill the interstices between almost spherical Aluminium matrix particles. This morphology was generated by growing percolating and highly intersecting small spherical inclusions of the matrix phase. This differed from the Cu-Fe case where fusible Cu was the grown phase. Again, the correlation function variance between real and RMG was comparable to the internal variance between real images at the same volume fraction. Images and information regarding the Sn-Al generated microstructures are shown below in Table 2.

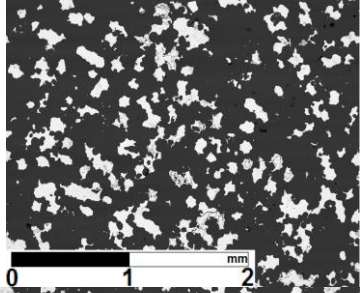
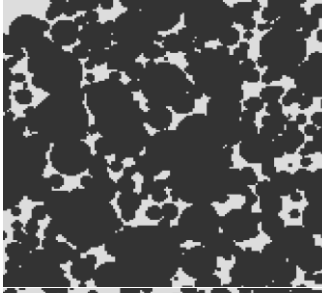
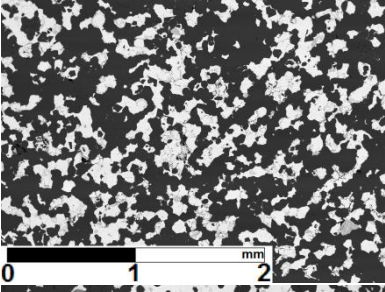
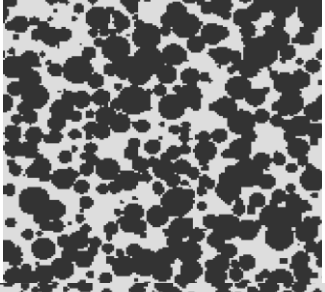
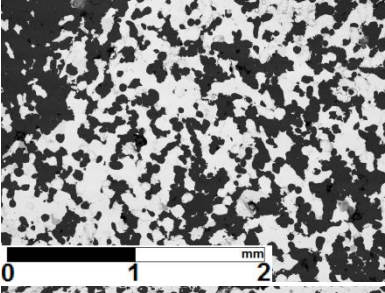
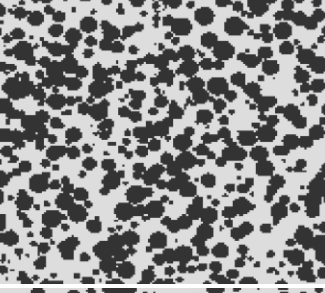
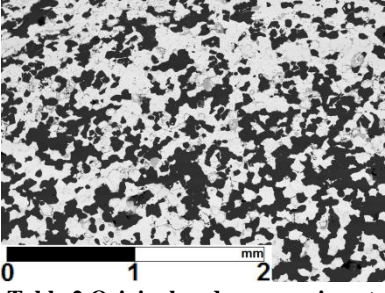
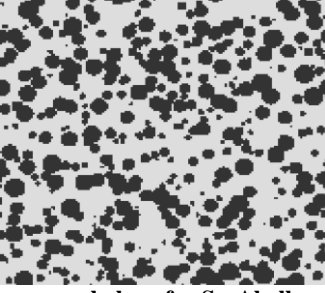
Original Microstructure	Generated Microstructure	Properties	Correlation Function Mean Variance Between Real Images	Correlation Function Mean Variance Between Real and Grown Images
		Alloy Properties: Sn-Al 20% Vf. Generation Properties: $\delta R = 75\%$ $I_n = 30\%$ $P_e = 30\%$	Radial Distribution: 6.93×10^{-4} Two Point: 7.37×10^{-4}	Radial Distribution: 2.2×10^{-4} Two Point: 5.19×10^{-5}
		Alloy Properties: Sn-Al 40% Vf. Generation Properties: $\delta R = 75\%$ $I_n = 30\%$ $P_e = 30\%$	Radial Distribution: 5.31×10^{-4} Two Point: 5.80×10^{-4}	Radial Distribution: 1.3×10^{-3} Two Point: 7.74×10^{-4}
		Alloy Properties: Sn-Al 50% Vf. Generation Properties: $\delta R = 75\%$ $I_n = 30\%$ $P_e = 30\%$	Radial Distribution: 1.9×10^{-2} Two Point: 2.0×10^{-2}	Radial Distribution: 1.2×10^{-3} Two Point: 1.14×10^{-4}
		Alloy Properties: Sn-Al 60% Vf. Generation Properties: $\delta R = 75\%$ $I_n = 30\%$ $P_e = 30\%$	Radial Distribution: 1.5×10^{-3} Two Point: 1.8×10^{-3}	Radial Distribution: 2.72×10^{-4} Two Point: 2.13×10^{-4}

Table 2 Original and grown microstructure morphology for Sn-Al alloys with the generation parameters δR being Radial Deviation, I_n Intersection allowance and P_e being likelihood to grow by percolation. The mean variance between the generated and the real image correlation functions is given along with the mean variance observed between real images.

The randomly grown Sn-Al microstructures were also of high quality. By observation, they closely represented the electron micrographs of the physical samples. This similarity is quantified in the correlation function mean variances. The real-real and real-grown mean variances were comparable for all volume fractions. It can be seen by comparison of the correlation function variances that the Cu-Fe type microstructures had a closer representation.

2.3 Effective Conductivity

The constituent thermal conductivities were taken from C. Y. Ho et. al. [5]. This temperature dependent data formed the constituent conductivities of each phase in the alloy microstructures. The differing microstructures were then simulated over a range of temperatures and the derived effective conductivity was recorded. The Cu-Fe data is displayed in Figure 7, whilst the Sn-Al data is presented in Figure 8. Additional tabulated data is presented in Appendix A.

Both materials simulated displayed a reduction in effective thermal conductivity with temperature similar to the constituent behaviour. The reduction in conductivity over the phase change is, as expected, more pronounced as the volume fraction of the fusible phase increases. The high effective thermal conductivity prior to phase change presents a significant benefit in allowable charging rate for a large volume of the material. The following results are valid to a maximum discrete particle size of 7 mm, above which natural convection may become significant in thermal transport.

The Cu-Fe temperature dependent effective conductivity for volume fractions up to 60% are shown in Figure 7. The Cu-Fe system had the high conductivity phase as the inclusion and hence the overall thermal conductivity increased with volume fraction. The thermal conductivity of the copper constituent demonstrates a near linear decrease to the phase change discontinuity whilst the Iron conductivity exhibits a minimum at 800 °C. For all volume fractions the solid effective conductivity decreased to the 800 °C minima, flattening as the volume fraction increased. Above the melting temperature of Copper both materials had a positive conductivity-temperature gradient and this behaviour has been mimicked in the effective property.

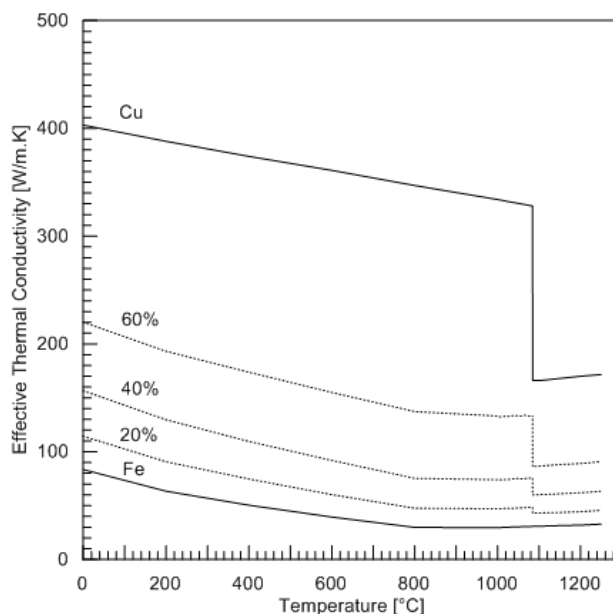


Figure 7 Effective thermal conductivity against temperature for Cu-Fe Volume fractions. Pure Copper and Iron are also shown for comparison. The melting temperatures of Copper and Iron are 1085 °C and 1538 °C respectively.

The temperature dependent effective conductivity of Sn-Al for volume fractions to 60% are shown in Figure 8. Aluminium is the more conductive material in the Sn-Al alloy and formed the matrix, thus the alloys effective conductivity dropped with increasing volume fraction of Sn. Solid Tin has a slightly concave up conductivity shape whilst Aluminium exhibits a maximum at 100 °C. The solid alloy effective conductivity thus varied from concave down, through a near linear decrease, to concave up as the Sn volume fraction increased. The conductivity-temperature gradient of the alloy above the melting temperature of Tin was found to decrease for low volume fractions and increase for higher volume fractions.

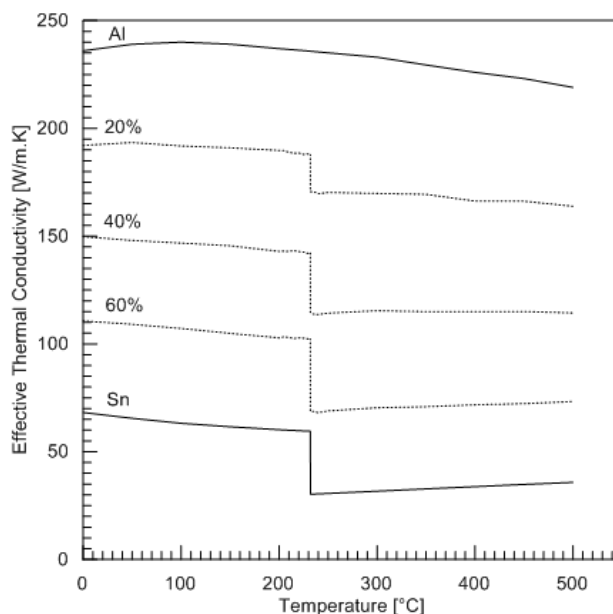


Figure 8 Effective thermal conductivity against temperature for Sn-Al Volume Fractions. Pure Aluminium and Tin are shown for comparison. The melting temperatures of Tin and Aluminium are 232 °C and 660 °C respectively.

A comparison was made to the statistical models of equations 1- 5 to ascertain whether they could be useful in predicting the effective MGA behaviour. The Cu-Fe composite was found to have an effective thermal conductivity similar to that predicted by the Maxwell-Euckman model at all temperatures and for volume fractions less than 50% Cu. At volume fractions of copper greater than or equal to 50% the Maxwell-Euckman model was found to be

inadequate. This is due to the assumption of the ME model that the discrete phase consists of randomly distributed *non-interacting* spheres. It can be observed in the microscope images of Table 1 that at 50% Cu volume fraction the onset of percolation began, causing the spheres to thermally interact with each other. The Bruggeman, Reciprocity and ME2 models over-predicted the conductivity, the latter model with the greatest divergence. The comparison is shown graphically in Figure 9 for a volume fraction of 40% Copper.

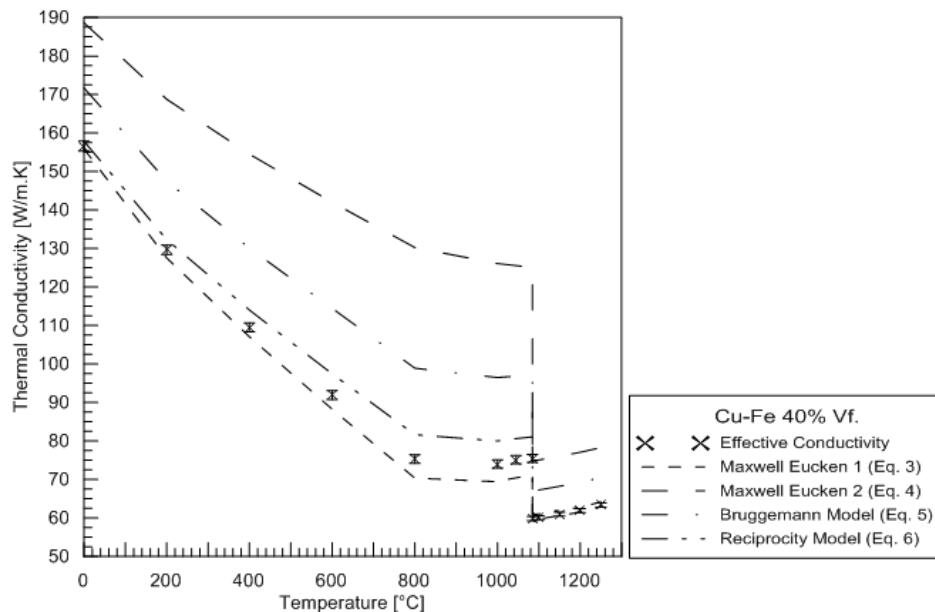


Figure 9 Statistical Model Estimation of effective conductivity for Cu-Fe 40%, the simulated data are crosses. The original Maxwell-Eucken 1 model best fitted the data.

The Sn-Al alloy morphology was dissimilar to the assumed structures of the statistical models discussed in this paper. The Maxwell models were derived on a distribution of non-interacting spherical inclusions or omissions, poorly matching the morphology of the Sn-Al alloys. The Reciprocity based model diverged less than the ME1 model but still gave a poor representation at all volume fractions save 50%. The Bruggeman model, based on an ideally isotropic case, gave a closer estimate than the Maxwell models but still gave errors greater than 5%. These results are shown in Figure 10 again for 40% volume fraction of inclusion material.

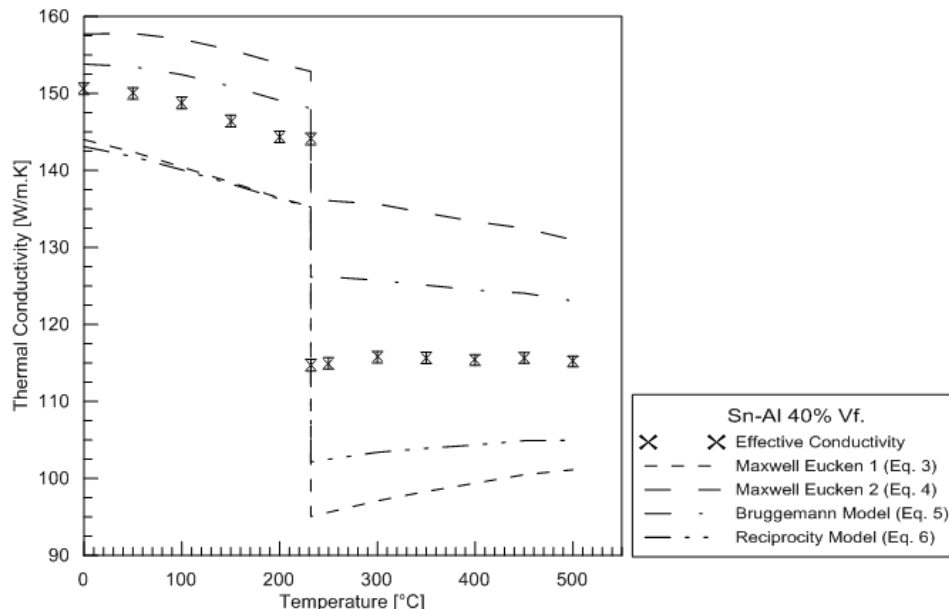


Figure 10 Statistical Model Estimation of effective conductivity for Sn-Al 40% the simulated data are crosses. None of the models could closely fit the data. The Bruggemann model was the best of those analysed.

In understanding how a microstructure might be optimised for effective thermal conductivity, a further study was undertaken. The ratio of effective conductivity may be normalised against the series solution to provide a *microstructural efficiency* (Eq. 6). This efficiency is a function both of the sample morphology and the ratio of constituent conductivities. The efficiency also depends on whether the more conductive constituent forms the inclusion or the matrix phase.

It was found that for a more conductive matrix a hard spheres type microstructure was more efficient than an interstices type microstructure. For a more conductive inclusion phase the interstice type morphology was more efficient. This suggests that the Cu-Fe alloy would benefit from being sintered above the melting temperature of copper, or by using less spherical copper powder. Inversely, the Sn-Al alloy would be more efficient if it had of been sintered below the melting temperature of Tin obtaining a more spherical inclusion shape. The difference is more noticeable for large conductivity ratios.

More generally, where the inclusion was more conductive the interstice type microstructure was more efficient over all volume fractions examined. This can be seen in Figure 11. Where the inclusion is less conductive, as seen in Figure 12, the microstructural efficiency of the hard spheres type microstructure is higher for all volume fractions tested. The difference is more pronounced as the inclusion conductivity increases. With increasing constituent conductivity ratio the microstructural efficiency is also seen to drop. It should be noted that microstructural efficiency must converge to unity at 0% and 100% volume fractions.

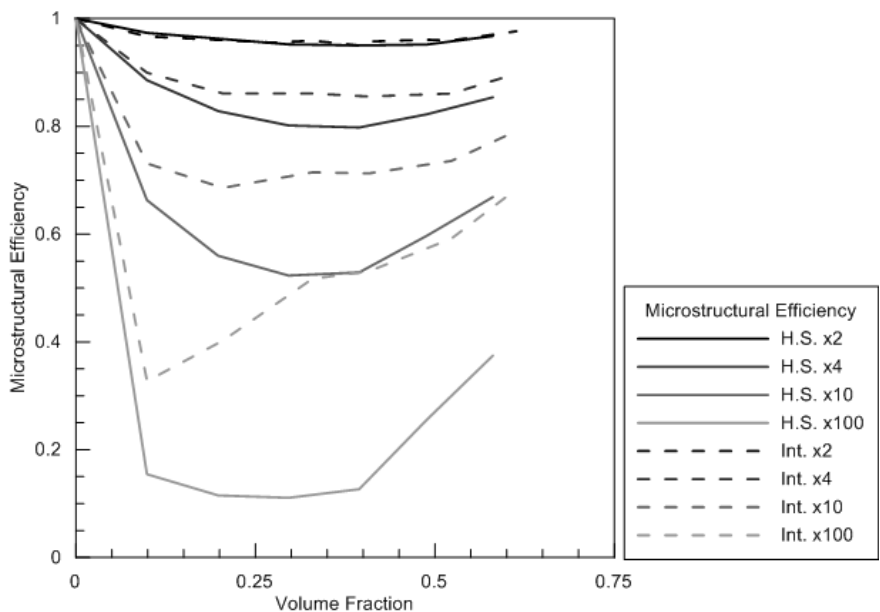


Figure 11 Microstructural efficiency of Hard Spheres (H.S.) and Interstices (Int.) for a range of volume fractions and four different ratios of inclusion to matrix conductivity. Here the inclusions are more conductive than the matrix.

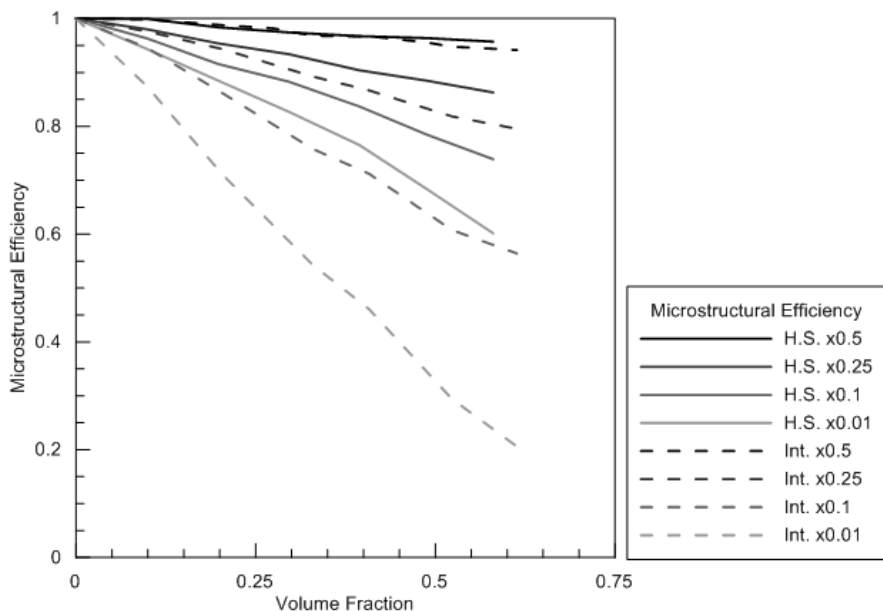


Figure 12 Microstructural efficiency of Hard Spheres (H.S.) and Interstices (Int.) for a range of volume fractions and four different ratios of inclusion to matrix conductivity. Here the inclusions are less conductive than the matrix.

3 Conclusions

The effective thermal conductivity for potential thermal storage media Cu-Fe and Sn-Al immiscible alloys have been estimated through a Lattice Monte Carlo (LMC) procedure. The physical threshold size for conduction dominated heat transfer in molten inclusions was determined to be less than 7 mm for the fusible phases. The computational alloy

microstructures were grown by calibrating a Random Microstructure Generation (RMG) algorithm to Optical and SEM microstructure images. The RMG and LMC processes were validated for physical similarity, mesh independence and periodicity. It was found that the Cu-Fe alloy would have a higher effective conductivity if it were sintered above the melting temperature of copper. Inversely, the Sn-Al alloy would have a higher effective conductivity if the Tin inclusions were spherical. Generally a low conductivity inclusion is more microstructurally efficient with a hard spheres microstructure morphology, whilst a high conducting inclusion is more efficient with an interstice type microstructure.

4 Acknowledgements

The authors of this paper would like to acknowledge the financial assistance of an Australian Postgraduate Award and an ARENA postgraduate scholarship. The Electron Microscope and X-Ray Unit of the University of Newcastle is also acknowledged for imaging services.

References

- [1] S. Khare, M. Dell'Amico, C. Knight, S. McGarry, Selection of materials for high temperature latent heat energy storage, *Solar Energy Materials & Solar Cells*, 107 (2012) 20-27.
- [2] A. Sharma, V.V. Tyagi, C.R. Chen, D. Uddhi, Review on thermal energy storage with phase change materials and applications, *Renewable and Sustainable Energy Reviews*, 13 (2009) 318-345.
- [3] B. Zalba, J. Marín, L. Cabeza, H. Mehling, Review on thermal energy storage with phase change: materials, heat transfer analysis and applications, *Applied Thermal Engineering*, 23 (2003) 251-283.
- [4] H. Sugo, E. Kisi, D. Cuskelly, Miscibility gap alloys with inverse microstructures and high thermal conductivity for high energy density thermal storage applications, *Applied Thermal Engineering*, 51 (2013) 1345-1350.
- [5] C.Y. Ho, R.W. Powell, P.E. Liley, Thermal Conductivity of the Elements, *Journal of Physical and Chemical Reference Data*, 1(2) (1972) 143.
- [6] Y.S. Touloukian, R.W. Powell, C.Y. Ho, M.C. Nicolaou, *Thermal Diffusivity*, 1974.
- [7] S. Torquato, *Random Heterogeneous Materials: Microstructure and Macroscopic Properties*, in, Springer, New York, 2002, pp. 1333-1356.
- [8] R.C. Progelhof, J.L. Throne, R.R. Ruetsch, Methods for Predicting the Thermal Conductivity of Composite Systems: A Review, *Polymer Engineering and Science*, 16(9) (1976) 615-625.
- [9] J. Wang, J.K. Carson, M.F. North, D.J. Cleland, A new approach to modelling the effective thermal conductivity of heterogeneous materials, *International Journal of Heat and Mass Transfer*, 49 (2006) 3075-3083.
- [10] A. Padilla, A. Sanchez-Solis, O. Manero, A Note on the Thermal Conductivity of Filled Polymers, *Journal of Composite Materials*, 22 (1987) 616-628.
- [11] A. Eucken, Allgemeine Gesetzmäßigkeiten für das Wärmeleitvermögen verschiedener Stoffarten und Aggregatzustände., *Forschung.*, 11 (1940) 6-20.
- [12] K.S. Reddy, P. Karthikeyan, Combinatory Models for Predicting the Effective Thermal Conductivity of Frozen and Unfrozen Food Materials, *Advances in Mechanical Engineering*, (2010).

- [13] D.A.G. Bruggeman, Berechnung verschiedener physikalischer Konstanten von heterogenen Substanzen, Dielectricitätskonstanten und Leitfähigkeiten der Mischkörper aus isotropen Substanzen, *Annalen der Physik*, 416 (1935).
- [14] J.A.d. Rio, R.W. Zimmerman, R.A. Dawe, Formula for the conductivity of a two-component material based on the reciprocity theorem, *Solid State Communications*, 106(4) (1998) 183-186.
- [15] J.B. Keller, A Theorem on the Conductivity of a Composite Medium, *Journal of Mathematical Physics*, 5(4) (1964) 548-549.
- [16] G. Murch, I. Belova, T. Fiedler, A. Öchsner, The Lattice Monte Carlo Method for Solving Phenomenological Mass and Heat Transport Problems, *diffusion-fundamentals*, 4 (2007) 15.11-15.23.
- [17] T. Fiedler, I.V. Belova, A. Öchsner, G.E. Murch, Lattice Monte Carlo Analysis of Thermal Diffusion in Multi-Phase Materials, in: *Heat Transfer in Multi-Phase Materials*, Springer, 2011, pp. 275-300.
- [18] C. Veyhl, T. Fiedler, O. Andersen, J. Meinert, T. Bernthaler, I.V. Belova, G.E. Murch, On the thermal conductivity of sintered metallic fibre structures, *International Journal of Heat and Mass Transfer*, 55(9-10) (2012) 2440-2448.
- [19] T. Fiedler, I.V. Belova, G.E. Murch, Theoretical and Lattice Monte Carlo analyses on thermal conduction in cellular metals, *Computational Materials Science*, 50 (2010) 503-509.
- [20] S. Ramaswamy, M. Gupta, A. Goel, U. Aaltosalmi, M. Kataja, A. Koponen, B.V. Ramarao, The 3D structure of fabric and its relationship to liquid and vapor transport, *Colloids and Surfaces A: Physicochemical Engineering Aspects*, 241 (2004) 323-333.
- [21] J.J. DeMarco, J.B. Smathers, C.M. Burnison, Q.K. Ncube, T.D. Solberg, CT-Based Dosimetry Calculations for ¹²⁵I Prostate Implants, *International Journal of Radiation Oncology, Biology and Physics*, 45(5) (1999) 1347-1353.
- [22] F. Incropera, D. Dewitt, T. Bergman, A. Lavine, *Fundamentals of heat and mass transfer*, Wiley & Sons, Inc., Hoboken, NJ, USA, 2006.
- [23] M. Chow, *An Experimental Investigation of Natural Convection Inside a Sphere*, Kansas State University, Kansas, 1973.
- [24] Y.-S. Lin, *An Experimental Study of Flow Patterns and Heat Transfer by Natural Convection Inside Cubical Enclosures*, Kansas State University, Manhattan, 1978.

Appendix (Tabulated Effective Thermal Conductivity Data)

Table 3 Effective Thermal Conductivity of Cu-Fe Alloy.

Volume Fraction of Copper

T [°C]	Effective Conductivity [W/m.K]															
	0%		10%		20%		30%		40%		50%		60%		100%	
0	83.5	± 1.67	97.3	± 2.32	114.4	± 2.96	133.7	± 3.6	156.6	± 4.24	186.0	± 4.88	220.2	± 5.52	403.0	± 8.06
250	59.7	± 1.2	72.7	± 1.92	86.7	± 2.57	103.4	± 3.23	124.7	± 3.88	155.0	± 4.53	188.3	± 4.53	384.4	± 7.68
500	44.8	± 0.9	55.3	± 2.41	67.5	± 3.81	82.0	± 5.21	100.1	± 6.61	113.0	± 8.01	146.1	± 9.41	368.0	± 14.7
750	30.8	± 0.62	40.8	± 1.93	50.8	± 3.26	62.9	± 4.6	79.5	± 5.93	108.7	± 7.26	141.7	± 8.59	350.4	± 14.0
1000	29.6	± 0.59	37.7	± 1.87	47.0	± 3.16	58.4	± 4.44	74.0	± 5.72	102.0	± 7.00	133.0	± 8.28	334.0	± 13.3
1084	30.7	± 2.46	39.0	± 3.53	48.3	± 4.60	60.1	± 5.67	75.5	± 6.74	102.9	± 7.81	133.2	± 8.88	328.0	± 13.1
1084	30.7	± 2.46	36.3	± 4.72	43.2	± 6.97	50.9	± 9.22	59.8	± 11.4	72.5	± 13.7	86.6	± 15.9	166.0	± 24.9
1250	32.8	± 2.62	39.0	± 4.95	45.7	± 7.27	53.5	± 9.59	63.4	± 11.9	76.6	± 14.2	90.8	± 16.5	171.6	± 25.7

Table 4 Effective Thermal Conductivity of Sn-Al Alloy.

Volume Fraction of Tin

T [°C]	Effective Conductivity [W/m.K]															
	0%		10%		20%		30%		40%		50%		60%		100%	
0	236.0	± 7.08	215.2	± 6.59	192.1	± 6.09	165.0	± 5.58	149.8	± 5.08	125.7	± 4.57	110.7	± 4.07	68.2	± 2.05
50	239.0	± 7.17	217.7	± 6.67	193.5	± 6.14	164.8	± 5.62	148.0	± 5.10	124.3	± 4.58	109.1	± 4.06	65.5	± 1.97
100	240.0	± 7.2	217.5	± 6.69	191.8	± 6.15	163.7	± 5.62	146.8	± 5.09	122.5	± 4.56	107.2	± 4.03	63.2	± 1.90
150	239.0	± 7.17	216.8	± 6.66	191.0	± 6.12	161.8	± 5.59	145.5	± 5.05	120.4	± 4.52	104.9	± 3.99	62.6	± 1.88
200	237.0	± 7.11	214.6	± 6.6	189.8	± 6.06	160.1	± 5.53	142.9	± 5.00	118.2	± 4.47	102.8	± 3.94	60.2	± 1.81
231	235.8	± 7.074	214.8	± 6.56	187.8	± 6.03	158.9	± 5.5	142.3	± 4.97	117.3	± 4.44	102.1	± 3.91	59.5	± 1.79
232	235.8	± 7.074	204.8	± 6.53	170.6	± 5.98	133.0	± 5.42	114.5	± 4.86	84.7	± 4.31	68.7	± 3.75	30.3	± 1.52
300	233.0	± 6.99	203.5	± 6.46	169.8	± 5.92	133.5	± 5.38	115.4	± 4.84	86.4	± 4.3	70.4	± 3.76	31.7	± 1.59